CHEMISTRY OF MATERIALS
Article

Chem. Mater. **2010,** *22,* 319–329 319
DOI:10.1021/cm902184m

Low Temperature Synthesis and Characterization of Nanocrystalline Titanium Carbide with Tunable Porous Architectures

David W. Flaherty,[†] R. Alan May,[‡] Sean P. Berglund,[†] Keith J. Stevenson,[‡] and C. Buddie Mullins*,[†]

[†]*Departments of Chemical Engineering and* [‡]*Chemistry and Biochemistry , Center for Electrochemistry, Texas Materials Institute, The University of Texas at Austin, 1 University Station, CO400 Austin, Texas, 78712*

Received July 17, 2009. Revised Manuscript Received November 14, 2009

High surface area, porous titanium carbide films have been synthesized at room temperature via reactive ballistic deposition (RBD). X-ray diffraction and X-ray photoelectron spectroscopy show that evaporative deposition of titanium in an ethylene ambient environment allows for low temperature (35 °C) synthesis of nanocrystalline titanium carbide, a material which typically requires high processing temperatures to produce. Angle-dependent RBD allows for the controlled tuning of TiC nanostructure and porosity where changing the deposition angle from near normal incidence (13°) to more glancing angles (50−85°) changes the film morphology from relatively nonporous, dense TiC to a continuous, reticulated TiC and finally to discrete, nanocolumnar TiC. The influence of the deposition angle on TiC optical constants, porosity, specific surface area, and the pore size distribution has been investigated using hybrid quartz crystal microbalance and ellipsometric porosimetry. Notably, TiC films deposited at 35 °C at an angle of 70° have a specific surface area of 710 $m^2 \cdot g^{-1}$ and a mean Kelvin radius of 1.8 nm, making them attractive materials for application in catalysis, energy conversion, and storage.

(I). Introduction

Transition metal carbides (TMCs) have attracted significant interest for a number of applications due to intrinsic material properties such as excellent thermal and chemical stability, high hardness, wear and corrosion resistance, and electrical conductivity.[1,2] Traditionally, these materials have been used as coatings for machining tools, rotors within gas turbines, burner tubes and tiles within furnaces, and as protective coatings within fusion reactors. Additionally, pioneering work by Boudart and co-workers demonstrated the platinum-like reactivity of tungsten carbide catalysts, after which many investigations have shown that TMCs catalyze a number of reactions (many at rates matching or exceeding the best known Group VIII transition metals) involving hydrogen transfer (hydrogenation, isomerization, hydrodesulfurization) and other chemical transformations.[3,4] Compared to Pt-group metals, TMCs have the added benefits of comparatively low cost, much greater natural abundance (of the raw transition metals), high thermal stability, and greater tolerance to common catalyst poisons.[2,5] Further, recent work by Gogotsi and co-workers has demonstrated that chlorination and subsequent etching of metal carbides yield high surface area, porous carbons which have shown great potential for use as electrical double layer capacitors or for hydrogen storage.[6,7]

Due to the wide range of applications for carbides, there is great interest in the development of preparation techniques suitable for specific applications. For example, in mechanical applications, thin, dense coatings are desired; however, TMCs synthesized for use in catalysis should possess high surface area and porosity. Regardless of the desired application, the preparation of carbides is frequently both time and energy intensive. Thorough reviews and discussions of many approaches have been compiled by Pierson[1] as well as Oyama.[2,8] In brief, a number of approaches exist which transform the transition metal (TM) precursor into the desired TMC product and which can be organized into several categories: solid-state reaction and diffusion processes, solid−gas reactions, chemical vapor deposition reactions, and liquid precursor or sol−gel reactions. All of these processes rely on high temperature synthesis or annealing to fully transform the material into the TMC (e.g., solid-state synthesis

*To whom correspondence should be addressed. E-mail: mullins@che.utexas.edu.

(1) Pierson, H. O. *Handbook of Refractory Carbides and Nitrides: Properties, Characteristics, Processing and Applications*; Noyes Publications: Westwood, N. J., 1996.
(2) Oyama, S. T., Ed. *The Chemistry of Transition Metal Carbides and Nitrides*; Blackie Academic and Professional: London, 1996.
(3) Levy, R. B.; Boudart, M. *Science* **1973**, *181*, 547–549.
(4) Oyama, S. T. *Catal. Today* **1992**, *15*, 179–200.
(5) Chen, J. G. *Chem. Rev.* **1996**, *96*, 1477–1498.
(6) Chmiola, J.; Yushin, G.; Gogotsi, Y.; Portet, C.; Simon, P.; Taberna, P. L. *Science* **2006**, *313*, 1760–1763.
(7) Gogotsi, Y.; Nikitin, A.; Ye, H. H.; Zhou, W.; Fischer, J. E.; Bo, Y.; Foley, H. C.; Barsoum, M. W. *Nat. Mater.* **2003**, *2*, 591–594.
(8) Oyama, S. T. *Catal. Today* **1992**, *15*, 179–200.

Published on Web 12/30/2009

techniques are conducted at temperatures as high as 1200−2000 °C). These extreme temperatures are necessary for a number of reasons. For example, carbothermal synthesis of TiC ($TiO_2 + C \rightarrow TiC + CO$) or self-propagating high-temperature synthesis ($Ti + C \rightarrow TiC$) require solid-state diffusion of carbon into metal-oxides or metals, thus requiring high temperatures in order to proceed at reasonable rates.[9,10] Other techniques require thermal decomposition of a stable precursor (CH_4, C_2H_2) over a relatively unreactive surface (bulk metal oxide or bulk metal passivated with native surface oxide). Generally, these approaches result in dense micrometer sized particles with low specific surface areas ($< 10\ m^2 \cdot g^{-1}$). There has been some success in creating high surface area TMCs utilizing high surface area metal oxide precursors. Ribeiro et al. employed temperature programmed reaction (TPR) of high surface area tungsten oxide with CH_4 and H_2 at 877 °C to produce W_2C with a specific surface area (SSA) of 100 $m^2 \cdot g^{-1}$.[11] Ledoux and co-workers have utilized shape memory synthesis[12] to create 140 $m^2 \cdot g^{-1}$ silicon carbide, greater than 200 $m^2 \cdot g^{-1}$ vanadium carbide (with residual carbon), and molybdenum and tungsten carbides with SSA as great as 100−200 $m^2 \cdot g^{-1}$.[13−15] Yu et al. have reported the synthesis of high surface area TiC-carbon composites with a SSA of 823 $m^2 \cdot g^{-1}$ formed from the carbothermal reduction of titanium citrate with a triblock copolymer template at 1000 °C which resulted in 4 to 5 nm TiC nanocrystals suspended in a mesoporous carbon matrix, with an overall stoichiometry of $\sim TiC_8$.[16]

Recently, procedures for lower temperature synthesis of titanium carbide have received greater attention. Lu et al. formed TiC at 450 °C by co-reduction of $TiCl_4$ and CCl_4 with sodium metal.[17] A similar technique was employed by Hu and co-workers to synthesize TiC powders by the simultaneous reduction and carburization of titanium dioxide by magnesium and magnesium carbonate at 550 °C and by Feng et al. who directly reacted $TiCl_4$ with CaC_2 at 500 °C.[18,19] Simultaneous reduction and carburization lead to the formation of powders with surface areas of $\sim 16\ m^2 \cdot g^{-1}$ and particle diameters of ~80 nm. Other approaches for the deposition of TiC have included a number of techniques based on laser ablation, arc evaporation, electron beam evaporation, or reactive plasma deposition.[2] These techniques combine fully reduced metal (e.g., Ti^0) with carbon on nanometer length scales which minimizes the role of solid-state diffusion. Low temperature synthesis (80−150 °C) of TiC by reactive sputtering of a titanium target has been reported by several investigators.[2,20,21] During this process, carbon can be incorporated by direct evaporation as in the case of Voevodin et al.[21] or by plasma induced decomposition of a hydrocarbon gas as used by Zehnder and Patscheider.[20] These two approaches lead to deposition of dense composite films of TiC which are accompanied by significant amounts of amorphous carbon (up to an overall stoichiometry of $Ti_{0.3}C_{0.7}$)[21] due to excess carbon deposition during synthesis. Johnson et al. synthesized dense thin films of TiC, Mo_2C, and W_2C by employing direct electron beam evaporation of carbon and metal sources resulting in the deposition of alternating carbon−metal layers 2−40 Å thick; however, the deposited films required annealing at elevated temperatures (350−600 °C) in order to form carbide.[22]

Alternatively, reactive ballistic deposition (RBD) can be utilized to deposit TiC films while providing control of the film's morphology, surface area, and porous architecture.[23−25] In ballistic or "hit and stick" deposition schemes, high surface area, porous films are prepared by deposition at oblique angles.[26] Topographically elevated points, created stochastically, preferentially intercept incoming atoms while shadowing lower regions.[27] This self-shadowing growth process results in nanostructured films whose porosity and morphology are determined largely by the angle of deposition and the kinetic energy of the incoming atoms.[28,29] However, in the RBD scheme, the metal is deposited in a reactive gas, greatly extending the number of materials that can be synthesized including metal oxides[23,24] and carbides.[25] In this case, polycrystalline TiC is deposited using physical vapor deposition of titanium metal in a gaseous ethylene ambient environment at 35 °C. Here, we demonstrate that, unlike other TiC deposition schemes, it is possible to tailor TiC optical constants, morphology, surface area, porosity, and pore size distribution via control of the deposition angle. Dense films, continuous reticulated structures, or well separated discrete nanocolumns can be prepared by simple variation of the incident angle of deposition.

(9) Koc, R. *J. Mater. Sci.* **1998**, *33*, 1049.
(10) Koc, R.; Folmer, J. S. *J. Mater. Sci.* **1997**, *32*, 3101.
(11) Ribeiro, F. H.; Betta, R. A. D.; Guskey, G. J.; Boudart, M. *Chem. Mater.* **1991**, *3*, 805–812.
(12) Direct reaction of the metal-oxide vapor−liquid phase with a high surface area solid carbon at 1200−1300 °C under vacuum.
(13) Keller, N.; Reiff, O.; Keller, V.; Ledoux, M. J. *Diamond Relat. Mater.* **2005**, *14*, 1353.
(14) Meunier, F.; Delporte, P.; Heinrich, B.; Bouchy, C.; Crouzet, C.; Pham-Huu, C.; Panissod, P.; Lerou, J. J.; Mills, P. L.; Ledoux, M. J. *J. Catal.* **1997**, *169*, 33.
(15) Ledoux, M. J.; Pham-Huu, C. *Catal. Today* **1992**, *15*, 263.
(16) Yu, T.; Deng, Y. H.; Wang, L.; Liu, R. L.; Zhang, L. J.; Tu, B.; Zhao, D. Y. Adv. Mater. **2007**, *19*, 2301−2306.
(17) Lu, Q.; Hu, J.; Tang, K.; Deng, B.; Qian, Y.; Zhou, G.; Liu, X. *Chem. Phys. Lett.* **1999**, *314*, 37–39.
(18) Ma, J.; Wu, M.; Du, Y.; Chen, S.; Li, G.; Hu, J. *Mater. Sci. Eng. B* **2008**, *153*, 96.
(19) Feng, X.; Bai, Y.-J.; Lü, B.; Wang, C.-G.; Liu, Y.-X.; Geng, G.-L.; Li, L. *J. Cryst. Growth* **2004**, *264*, 316–319.
(20) Zehnder, T.; Patscheider, J. *Surf. Coat. Technol.* **2000**, *133−134*, 138–144.
(21) Voevodin, A. A.; Prasad, S. V.; Zabinski, J. S. *J. Appl. Phys.* **1997**, *82*, 855–858.
(22) Johnson, C.; Sellinschegg, H.; Johnson, D. C. *Chem. Mater.* **2001**, *13*, 3876–3881.
(23) Dohnálek, Z.; Kimmel, G. A.; McCready, D. E.; Young, J. S.; Dohnalkova, A.; Smith, R. S.; Kay, B. D. *J. Phys. Chem. B* **2002**, *106*, 3526–3529.
(24) Flaherty, D. W.; Dohnalek, Z.; Dohnalkova, A.; Arey, B. W.; McCready, D. E.; Ponnusamy, N.; Mullins, C. B.; Kay, B. D. *J. Phys. Chem. C* **2007**, *111*, 4765–4773.
(25) Flaherty, D. W.; Hahn, N. T.; Ferrer, D.; Engstrom, T. R.; Tanaka, P. L.; Mullins, C. B. *J. Phys. Chem. C* **2009**, *113*, 12742–12752.
(26) Barabási, A.-L.; Stanley, H. E. *Fractal Concepts in Surface Growth*; Cambridge University Press: Cambridge, Great Britain, 1995.
(27) Abelmann, L.; Lodder, C. *Thin Solid Films* **1997**, *305*, 1–21.
(28) Robbie, K.; Sit, J. C.; Brett, M. J *J. Vac. Sci. Technol., B* **1998**, *16*, 1115–1122.
(29) Kim, J.; Dohnálek, Z.; Kay, B. D. *Surf. Sci.* **2005**, *586*, 137–145.

While RBD is highly flexible and capable of growing a wide variety of nanostructured, porous materials, the extremely porous architecture and small quantity produced make them difficult to characterize with many common techniques which lack either the scope [e.g., atomic force microscopy (AFM) and transmission electron microscopy (TEM)] or sensitivity [e.g., scanning electron microscopy (SEM) and traditional gas physisorption measurements] to provide thorough characterization. This complicates the direct assessment of the physicochemical-morphological properties of high surface area, porous thin films deposited in this manner, and prior characterization has relied on complex and expensive ultrahigh vacuum (UHV) techniques.[23−25,29−32] However, even these complex UHV methods are incapable of quantifying how the film deposition angle affects the characteristic size of pores within the films, a property especially important for heterogeneous catalysis or electrochemical energy conversion and storage applications. To investigate this dependence, TiC was deposited directly on quartz crystals which allowed simultaneous acquisition of the mass change using the quartz crystal microbalance (QCM) technique[33] and measurement of changes in the film's optical properties via ellipsometry.[34,35] This new characterization technique provides a straightforward route for performing quantitative porosimetry measurements, demonstrating that the morphology, refractive index, SSA, and pore size distribution (PSD) of TiC films synthesized at room temperature can be tightly controlled by modification of the deposition angle during reactive ballistic deposition.[36]

(II). Experimental Section

TiC Film Synthesis. Titanium carbide films were deposited using the reactive ballistic deposition scheme described above and elsewhere.[25] Briefly, the films were synthesized in a high vacuum chamber equipped with electron beam evaporators (Omicrometer EFM3), an *x*-*y*-*z* sample manipulator mounted upon a rotary seal, two quartz crystal microbalances (RQCM, Inficon/Maxtek Inc.), a residual gas analyzer (Stanford Research Systems, RGA 200), and a sample holder which can be controlled to temperatures ranging from −196 to 900 °C (measured by a type K thermocouple) through a combination of liquid nitrogen cooling and resistive heating. The chamber base pressure was typically $\sim 7 \times 10^{-9}$ mbar. The electron beam evaporator was used to deposit metallic titanium onto Si(100) and quartz crystal microbalances held at 35 °C in an ethylene atmosphere of $\sim 2.5 \times 10^{-7}$ mbar. Following deposition, the TiC films were passivated in low pressure oxygen (6×10^{-5} mbar) before removal from the vacuum system. Greater detail concerning sample synthesis can be found in the Supporting Information.

Spectroscopic Ellipsometry (SE). Ellipsometry measurements at 60°, 65°, and 70° with wavelengths from 200 to 1000 nm were acquired on a J. A. Woolam M-2000 variable angle spectroscopic ellipsometer. The acquired ellipsometric parameters Ψ and Δ were transformed into the thickness of the deposited TiC films as well as the real, n, and imaginary, k, components of the complex refractive index using an optical model consisting of two layers, the Au substrate and the TiC film. RBD deposited films typically possess structural anisotropy which is difficult to account for with standard ellipsometry.[37,38] To simplify the model for this system, all SE measurements were taken with the sample oriented such that the deposition direction is parallel to the incident light beam and the data was fit using an isotropic model consisting of three Lorentzian oscillators. This sample orientation minimizes contributions from film anisotropy, as shown on several materials grown by deposition at glancing angles.[37,38] Each sample was fit for the film thickness in addition to the amplitude and broadening of these oscillators. Representative fit parameters and fits to ellipsometry data are provided in the Supporting Information, Figure S2.

Porosimetry. The apparatus for conducting porosimetry experiments has been described previously.[39] Porosimetry measurements were carried out in a hemicylindrical quartz flow cell in which the partial pressure of toluene was controlled ($P/P_o \pm 0.1\%$) by mixing of a stream of dry N_2 (99.9%) with a stream of toluene-saturated N_2 using high-precision Inficon digital flow controllers, model P8A. Adsorption and desorption isotherms of toluene on QCM−supported TiC films were acquired by simultaneous measurements of the mass change of adsorbate and the SE parameters Ψ and Δ, with respect to toluene partial pressure. Prior to the porosimetry runs, the films were degassed under flowing N_2 at ambient temperature until the QCM response stabilized (∼20 min); then, the dry N_2 stream was heated to 70 °C for ∼30 min until the resonant frequency of the QCM, f_R, again stabilized. The film was judged to be in equilibrium with the predetermined partial pressure of toluene by monitoring the change in f_R over time. Changes in f_R measured by the QCM were converted to mass using the Sauerbrey equation which is valid for rigid, evenly distributed deposits in air or vacuum within ∼5% of the crystal resonant frequency, conditions which were met in this study.[40] Changes in the ellipsometric values, Ψ and Δ, were much more difficult to interpret and are discussed in later sections.

X-ray Diffraction (XRD). X-ray diffraction measurements were acquired in a glancing incidence, detector scan geometry using a Bruker-Nonius D8 advanced diffractometer. The Cu Kα radiation source was operated at 40 kV and 40 mA while a nickel foil filter was used to screen out Cu Kβ radiation. All measurements were carried out in the $\theta/2\theta$ mode with an incident angle of radiation of 1°. The 2θ scan data were collected using a scintillation detector at 0.01° intervals over the range of 20−80° and a scan rate of 12° min^{-1}. Diffraction features were compared to the powder diffraction files (PDF) widely available for

(30) Dohnálek, Z.; Kimmel, G. A.; Ayotte, P.; Smith, R. S.; Kay, B. D. *J. Chem. Phys.* **2003**, *118*, 364–372.
(31) Kimmel, G. A.; Stevenson, K. P.; Dohnálek, Z.; Smith, R. S.; Kay, B. D. *J. Chem. Phys.* **2001**, *114*, 5284–5294.
(32) Cholette, F.; Zubkov, T.; Smith, R. S.; Dohnalek, Z.; Kay, B. D.; Ayotte, P. *J. Phys. Chem. B* **2009**, *113*, 4131–4140.
(33) Borras, A.; Sanchez-Valencia, J. R.; Garrido-Molinero, J.; Barranco, A.; Gonzalez-Elipe, A. R. *Microporous Mesoporous Mater.* **2009**, *118*, 314–324.
(34) Castro, Y.; Julian, B.; Boissiere, C.; Viana, B.; Amenitsch, H.; Grosso, D.; Sanchez, C. *Nanotechnology* **2007**, *18*, 7.
(35) Baklanov, M. R.; Mogilnikov, K. P.; Polovinkin, V. G.; Dultsev, F. N. *J. Vac. Sci. Technol., B* **2000**, *18*, 1385–1391.
(36) Rouessac, V.; van der Lee, A.; Bosc, F.; Durand, J.; Ayral, A. *Microporous Mesoporous Mater.* **2008**, *111*, 417–428.
(37) Schmidt, D.; Booso, B.; Hofmann, T.; Schubert, E.; Sarangan, A.; Schubert, M. *Opt. Lett.* **2009**, *34*, 992–994.
(38) Schmidt, D.; Booso, B.; Hofmann, T.; Schubert, E.; Sarangan, A.; Schubert, M. *Appl. Phys. Lett.* **2009**, *94*, 3.
(39) May, R. A.; Patel, M. N.; Johnston, K. P.; Stevenson, K. J. *Langmuir* **2009**, *25*, 4498–4509.
(40) Sauerbrey, G. *Z. Phys.* **1959**, *155*, 206–222.

each structure; TiC (PDF # 71−0298), Ti (PDF # 44−1294), Si (PDF # 75−0589), SiC (PDF # 73−2083), and SiO_2 (PDF #70−2539). Additionally, diffraction patterns were compared to those of graphite and other carbon composites as well as titanium oxides.

Scanning Electron Microscopy (SEM). Scanning electron micrographs are obtained using a LEO 1530 SEM. A primary electron beam energy of 20 kV and aperture of 30 μm were utilized for capturing images of the titanium carbide films deposited on Si(100) substrates. Profile SEM images were acquired by cleaving a substrate with a deposited TiC film and examining the freshly exposed edge.

X-ray Photoelectron Spectroscopy (XPS). X-ray photoelectron spectra were taken using the Kratos AXIS Ultra DLD model spectrometer using Mg Kα radiation. Argon ion sputtering (3 kV, 60 $\mu A \cdot cm^{-2}$) at 45° was used to clean the sample by removing the adventitious carbon and native oxide which formed when transferring TiC samples to the XPS system. XPS spectra were acquired for the Ti 2p, C 1s, and O 1s peaks both before and after sputtering the sample. Concentrations of Ti, C, and O were calculated by multiplying the integrated peak areas, obtained after subtracting a Shirley background,[41] for each individual element by their respective sensitivity factor (2.001, 0.278, and 0.780) as supplied by the manufacturer.

Annealing and Carburization. Titanium carbide films deposited by RBD were heated within a quartz tube mounted in a Carbomax furnace. Two MKS flow controllers were used to manipulate the flow rate of two gas mixtures utilized during annealing. TiC films deposited on Si(100) wafers were heated in 500 sccm flow of 10% CH_4/90% H_2 to the selected temperature (327, 827, and 1027 °C). The samples were held at the maximum temperature for ~3 h to allow for any changes in structure or composition. The samples were then cooled to near room temperature, after which the gas flow was switched to a 0.5% O_2/99.5% Ar mixture to gently passivate the surface of the films and minimize oxidation on exposure to air. Titanium foil samples (99.9%, 10 mm × 10 mm × 0.5 mm, MTI Corporation) and clean Si(100) wafers were heated simultaneously with the TiC samples. The titanium foil was carburized by temperature programmed reaction (TPR) with the CH_4 and H_2 gas mixture,[2,8] and the resulting bulk TiC sample served as a control for XRD and XPS measurements. The clean Si(100) wafer served as a control to identify contributions to XRD patterns originating from the substrate.

(III). Results

(A). Film Morphology and Composition. Figure 1 displays SEM images illustrating the profile and top views of the as-deposited TiC films grown by depositing 500 monolayers of titanium at 35 °C in an ethylene background pressure of 2.5×10^{-7} mbar with deposition angles of 13°, 50°, 60°, 70°, 80°, and 85°. It is clear from this work, and previous investigations, that the morphology of the deposited films is sensitive to the deposition angle during film growth.[23−25,28−31,42−53] As the deposition angle is gradually increased from 13° (near perpendicular to the surface) to 85° (near parallel to the surface), the film morphology evolves from a relatively dense material into a continuous, reticular structure and finally into arrays of discrete columns with characteristic diameters greater than 50 nm. At deposition angles of 70° and higher, nanometer scale voids are resolved by SEM in profile and top-down views. These changes are also reflected in the optical constants derived by SE for identical amounts of TiC deposited at angles ranging from 13 to 80° within the quartz cell under dry N_2 flow, Figure 2. The real, n, and imaginary, k, refractive indices of the films decrease as the deposition angle increases, concomitant with an increase in the volume fraction of voids. To a first approximation, this occurs because of a volume averaged blending of the refractive indices of TiC, $n \sim 3.2$, and N_2, $n \sim 1.0$. This is the essence of effective medium approximations through which the refractive index of a material can be determined from the refractive indices of its constituent parts. For example, values of n and k for TiC 13° (throughout the remainder of the paper TiC $XY°$ indicates a TiC film deposited at a deposition angle of $XY°$) were combined with a void layer

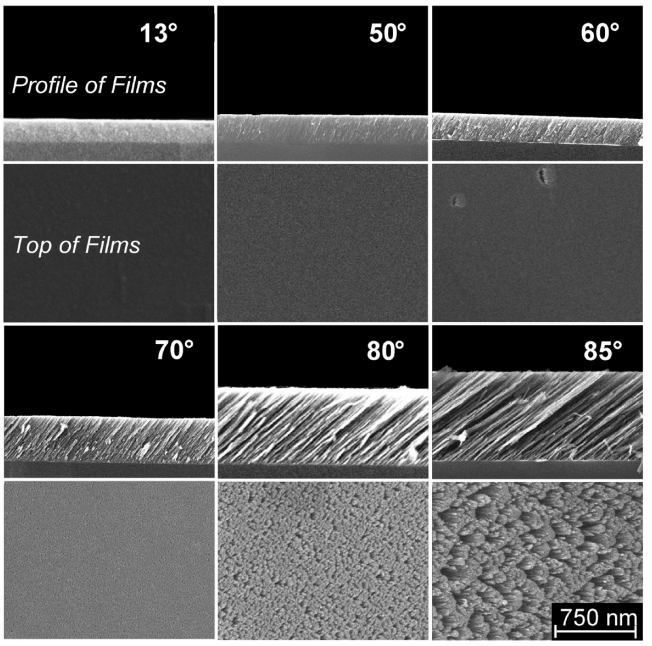

Figure 1. Scanning electron micrographs of TiC films grown by depositing 500 monolayers of titanium in an ethylene background at 2.5×10^{-7} mbar onto Si(100). Films were deposited at angles ranging from 13° to 85° at 35 °C.

(41) Shirley, D. A. *Phys. Rev. B* **1972**, *5*, 4709–4714.
(42) Kimmel, G. A.; Dohnálek, Z.; Stevenson, K. P.; Smith, R. S.; Kay, B. D. *J. Chem. Phys.* **2001**, *114*, 5295–5303.
(43) Robbie, K.; Brett, M. J.; Lakhtakia, A. *Nature* **1996**, *384*, 616.
(44) Robbie, K.; Friedrich, L. J.; Dew, S. K.; Smy, T.; Brett, M. J. *J. Vac. Sci. Technol., A* **1995**, *13*, 1032–1035.
(45) Sit, J. C.; Vick, D.; Robbie, K.; Brett, M. J. *J. Mater. Res.* **1999**, *14*, 1197.
(46) Smy, T.; Vick, D.; Brett, M. J.; Dew, S. K.; Wu, A. T.; Sit, J. C.; Harris, K. D. *J. Vac. Sci. Technol., A* **2000**, *18*, 2507–2512.
(47) Liu, F.; Umlor, M. T.; Shen, L.; Weston, J.; Eads, W.; Barnard, J. A.; Mankey, G. J. *J. App. Phys.* **1999**, *85*, 5486.
(48) Colgan, M. J.; Djurfors, B.; Ivery, D. J.; Brett, M. J. *Thin Solid Films* **2004**, *466*, 92–96.
(49) Harris, K. D.; McBride, J. R.; Nietering, K. E.; Brett, M. J. *Sens. Mater.* **2001**, *13*, 225.
(50) Motohiro, T.; Taga, Y. *Appl. Opt.* **1989**, *28*, 2466–2482.
(51) Messier, R.; Venugopal, V. C.; Sunal, P. D. *J. Vac. Sci. Technol., A* **2000**, *18*, 1538.
(52) Seto, M. W.; Robbie, K.; Vick, D.; Brett, M. J.; Kuhn, L. *J. Vac. Sci. Technol., B* **1999**, *17*, 2172.
(53) Stevenson, K. P.; Kimmel, G. A.; Dohnálek, Z.; Smith, R. S.; Kay, B. D. *Science* **1999**, *283*, 1505–1507.

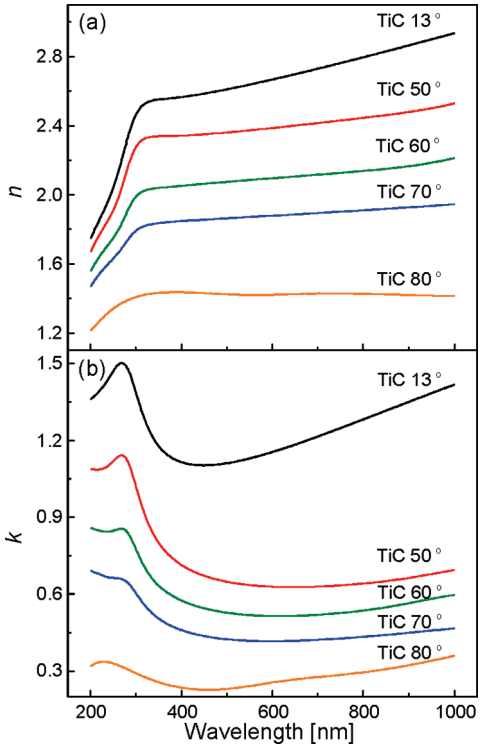

Figure 2. (a) Real, n, and (b) imaginary, k, portions of the complex refractive index derived using an isotropic approximation. Both n and k decrease with an increasing deposition angle due to the increasing film porosity.

($n = 1$, $k = 0$) using the Bruggeman effective medium approximation (BEMA)[54] to measure the porosity controlled by varying the deposition angle for each film. The BEMA method relates a composite material's refractive index to the known refractive indices of its individual components, thus yielding the volume fraction of each constituent.[54] This approach provided results within a few percent of those determined using the QCM measured film mass and SE derived film thickness. The angular dependence of the porosity (calculated from the mass of TiC as measured by QCM and the film thickness as measured by SE) of films deposited by related glancing angle deposition techniques is displayed in the Supporting Information, Figure S3, and closely follows the predictive model developed by Poxson et al.[55]

X-ray diffraction measurements indicate that the films, as-deposited at 35 °C, are crystalline. This is in stark contrast to the high temperatures required by other synthesis techniques as described earlier. Figure 3 shows XRD patterns acquired from a TiC film grown via RBD at 13° (nominally dense) as-deposited and annealed to each indicated temperature. Analysis of the diffraction patterns reveal the presence of a number of diffraction features from TiC indicated by blue arrows, corresponding to the (111), (200), (220), (311), and (222) crystal planes. (The diffraction pattern for a carburized titanium foil is provided in Supporting Information, Figure S4.)

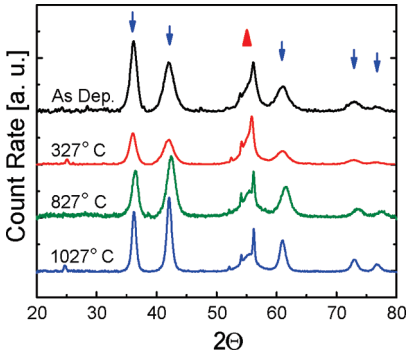

Figure 3. X-ray diffraction patterns for a TiC films deposited on Si(100) substrates at 35 °C with deposition angles of 13°. The film was incrementally annealed to 327, 827, and 1027 °C. Annealing the film leads to preferential growth of the crystallites along the (200) crystallographic plane.

Additionally, several features originating from the Si(100) substrate and its thermal oxide, SiO_2, are apparent within the range of 45−58° and are designated with a red triangle. No diffraction features indicative of metallic titanium, graphite, or other forms of carbon were observed for TiC films deposited by RBD. Although the TiC films adsorb large quantities of oxygen during passivation and exposure to air, no features corresponding to titanium oxide phases were observed. Since exposure to oxygen occurs at room temperature, the interaction of oxygen with the TiC film forms an amorphous oxycarbide overlayer as shown in XPS spectra, Figure S5 in the Supporting Information. Additionally, TiC films were grown by deposition at angles ranging from 50 to 85°, XRD patterns displayed in the Supporting Information, Figure S6. The carburized titanium foil sample provides a basis of comparison for Scherrer analysis of the XRD peak broadening.[56] This analysis indicates that the mean crystallite grain size within each columnar or reticulated TiC film ranges from 9.9 to 6.9 nm, with the average size decreasing with increasing deposition angle and film porosity. As seen in Figure 3, annealing is unnecessary for the formation of crystalline TiC; however, the relative intensities of the diffraction peaks change with annealing, showing a preferential nucleation and alignment along the (200) crystal plane. The (200) plane is the predominant diffraction feature in bulk TiC samples. The TiC diffraction peaks also become sharper, indicating an increase of crystallite size from ~10 nm for the as-deposited film at 35 °C to ~12 nm after annealing to 827 °C and finally to ~18 nm after annealing to 1027 °C. Average grain sizes for annealed films as derived from Scherrer analysis are summarized in the Supporting Information, Table S1, as a function of deposition angle and annealing conditions.

SEM images of TiC deposited at an angle of 85° were acquired after annealing in order to capture temperature induced changes in morphology, shown in Figure 4. Films deposited at 85° from normal incidence represent the most thermodynamically unstable films due to their high surface to volume ratio, due to the long free-standing

(54) Tompkins, H. G.; McGahan, W. A. *Spectroscopic Ellipsometry and Reflectometry*; Wiley-Interscience: New York, 1999.
(55) Poxson, D. J.; Mont, F. W.; Schubert, M. F.; Kim, J. K.; Schubert, E. F. *Appl. Phys. Lett.* **2008**, *93*, 3.
(56) Guinebretiere, R. *X-ray Diffraction by Polycrystalline Materials*; ISTE USA: Newport Beach, CA, 2007.

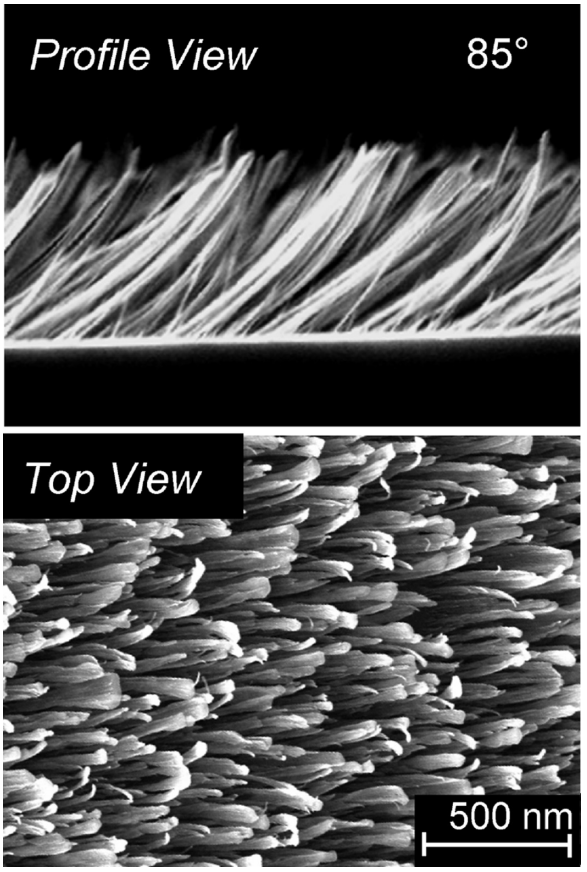

Figure 4. Scanning electron microscopy profile and top views of TiC film deposited at 85° and annealed to 827 °C.

nanocolumns. Annealing to 327 °C leads to no visual changes observable by SEM (not shown), but when the film is annealed to 827 °C, subtle changes can be seen in the fine structure of the nanocolumns when compared to the images in Figure 1. The annealing treatment likely leads to a slight smoothing of the rough surfaces of the nanocolumns concomitant with some densification and loss of surface area, as has been observed upon annealing in vacuum.[25] Morphological changes observed using SEM correlate to structural changes observed in XRD for films annealed at 827 °C. However, while the shape and roughness of individual columns changes, the film maintains its nanocolumnar morphology. In general, appreciable bulk diffusion rates are necessary for changes in morphology or sintering to occur in structured materials. The onset of bulk diffusion of solids typically coincides with the Tamman temperature (approximately one-half the value of the melting temperature).[57] Therefore, while we directly observe that the nonequilibrium structures seen here remain kinetically "trapped" or frozen even after annealing to 827 °C, it is not surprising since bulk TiC has a melting point of 3067 °C.[1]

X-ray diffraction of the polycrystalline Ti foil (MTI Corporation) was conducted after each carburization step (diffraction patterns are provided in the Supporting Information, Figure S4). Scherrer analysis of the as received Ti foil resulted in a calculated mean grain size

(57) Baerns, M., Ed. *Basic Principles in Applied Catalysis*; Springer-Verlag: Berlin, 2004.

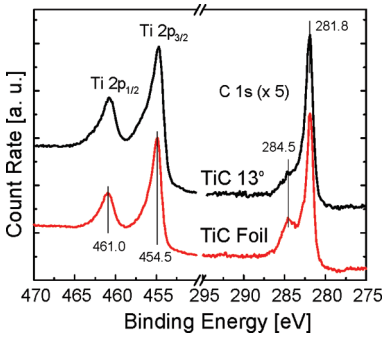

Figure 5. X-ray photoelectron spectra of the TiC 13° film and the carburized titanium foil, TiC foil. The Ti $2p_{1/2}$ and Ti $2p_{3/2}$ peaks closely resemble metallic titanium with the exception of a small shoulder at higher binding energies, suggesting a small degree of oxidation. The C 1s features at 284.5 and 281.8 eV correspond to graphitic and carbidic carbon, respectively. It is clear that the TiC 13° film synthesized by RBD contains a smaller amount of graphitic carbon than the TiC foil prepared by the TPR technique.

greater than or equal to ~60 nm. (A value that approaches the upper limit for Scherrer analysis due to the relative uncertainty introduced by peak broadening.) After carburization treatment of the foil at 327 °C, the diffraction pattern did not show any evidence of TiC, carbon, or narrowing of the Ti diffraction features. Treatment at 827 °C resulted in the formation of titanium carbide and an unidentified phase observed by additional diffraction peaks at 33.6°, 49.7°, and 65.6°. Diffraction features from metallic titanium were still apparent and are likely due to large amounts of titanium which remain beneath an outer layer of carbide. This illustrates the typical difficulty associated with synthesizing TMCs, that is, the necessity to overcome large kinetic barriers for solid-state diffusion of carbon into the host metal. Carburization at 1027 °C was necessary to achieve formation of pure titanium carbide and the complete disappearance of all titanium metal diffraction features.

X-ray photoelectron spectroscopy was employed to probe the chemical state of carbon within the TiC samples. Figure 5 displays XPS spectra acquired from the bulk of the TiC foil (prepared by TPR as described previously) and an as-deposited TiC 13° film. Due to the presence of adventitious carbon and surface oxide, argon ions were used to remove 5−10 nm of material from each sample's surface while monitoring the C 1s and O 1s features. When the C 1s and O 1s peaks became independent of sputter time, we expect that XPS spectra are representative of the bulk material. Overall, the estimated bulk atomic composition of the TiC foil is 38% titanium, 50% carbon, and 12% oxygen while the TiC 13° film bulk is 40% titanium, 31% carbon, and 28% oxygen, respectively. The relatively high oxygen content of both samples is due to the oxophilic nature of TiC. Indeed, all transition metal carbides have a high affinity for oxygen.[1] The TiC 13° film does contain a small fraction of micropores, as described later, which facilitate oxygen diffusion into the film upon exposure to air. The titanium $2p_{1/2}$ and $2p_{3/2}$ peaks, located at 461.0 and 454.5 eV, respectively, of both the TiC foil and the TiC 13° are very similar and indicate that the majority of titanium is nearly zerovalent. Carbon

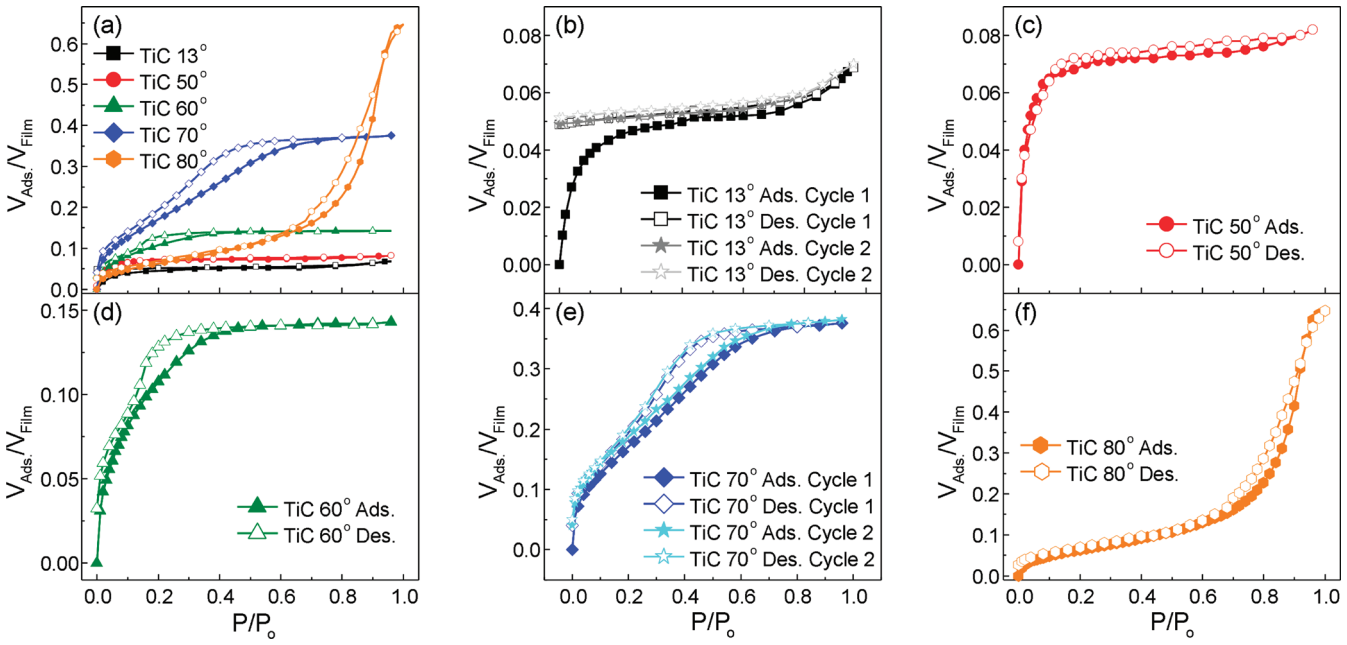

Figure 6. Volume fraction of adsorbate versus the film volume determined for toluene isotherms on TiC films deposited at various angles. (a) Overlay of all angles indicating the relative magnitude of adsorption, along with individual isotherms, filled symbols are the adsorption branch and empty symbols the desorption branch of the isotherm: (b) 13°(■), (c) 50°(●), (d) 60°(▲), (e) 70°(♦), and (f) 80° (⬢). Another subsequent isotherm was performed on all samples, but all except the 13° and 70° have been omitted for clarity.

is more electronegative than titanium which leads to the expectation of charge donation from titanium to carbon. However, the Ti−C bond is largely covalent in nature with only a small degree of ionic character, and estimates place the charge transfer at less than 0.5 electrons per titanium cation.[1,58] There are significant differences between the carbon 1s features of the TiC foil and TiC 13°. The TiC foil displays two distinct peaks at 284.5 and 281.8 eV. The peak at 281.8 eV corresponds to carbidic carbon and has been reported in previous XPS investigations of TiC while the feature at 284.5 eV is very close to the expected position for graphitic carbon deposits.[2,20,59] These peaks are fitted with Gaussians and deconvoluted to determine the relative percentage of graphitic and carbidic carbon. The TiC foil prepared by TPR is determined to have ~30% graphitic carbon and ~70% carbidic carbon. Interestingly, similar analysis of the TiC 13° film indicates that its carbon content is ~18% graphitic and ~82% carbidic. Rodriguez et al. utilized high resolution photoelectron emission spectroscopy of oxygen atom adsorption on a TiC(001) single crystal surface to show that very small oxygen exposures (10 Langmuirs or 1.33×10^{-5} mbar·sec) at 300 K induces chemical shifts of the C 1s peak similar in intensity to those in Figure 5.[60] This suggests that even trace residual gases within the XPS analysis chamber (H_2O, O_2, CO, and CO_2) may be responsible in part for deviations from a purely carbidic carbon state. These results provide further evidence that reactive ballistic deposition of titanium within the ethylene ambient environment result in the formation of TiC even at temperatures as low as 35 °C.

(B). Film Porosity, Surface Area, and Pore Size Measurements. Toluene adsorption isotherms were obtained via QCM porosimetry for films deposited at angles ranging from 13 to 80° and are presented in Figure 6. As seen in Figure 6, the volume fraction of adsorbed toluene as well as the partial pressure at which the adsorption−desorption hysteresis occurs increase with increasing deposition angle indicating that both the total capacity for toluene adsorption and the mean pore diameter increase with deposition angle. At larger deposition angles, the ultimate amount of adsorbate relative to the film volume increases while the onset of significant absorbance is shifted to larger values of P/P_o. The sample deposited at 13° (Figure 6b) was expected to be nonporous in which case the film would exhibit a Type II adsorption isotherm, concave adsorption relative to the x-axis followed by increased adsorption at high partial pressures due to multilayer formation, consistent with adsorption on nonporous surfaces.[61,62] However, the isotherm demonstrates Type I behavior, characterized by relatively large adsorption at low partial pressures followed by a region of constant adsorption at moderate partial pressures.[62] Type I isotherms typically arise from adsorption onto a microporous (pores < 2 nm in diameter) surface, though they can also arise from very strong attraction between the adsorbate and the surface leading to monolayer formation at very low partial pressures. Here, the Type I isotherm arises because of the presence of micropores as the mass detected at $P/P_o = 0.1$ is ~100 times

(58) Oyama, S. T. *J. Solid State Chem.* **1992**, *96*, 442–445.
(59) Ju, Z.; Fan, N.; Ma, X.; Li, J.; Ma, X.; Xu, L.; Qian, Y. *J. Phys. Chem. C* **2007**, *111*, 16202.
(60) Rodriguez, J. A.; Liu, P.; Dvorak, J.; Jirsak, T.; Gomes, J.; Takahashi, Y.; Nakamura, K. *J. Chem. Phys.* **2004**, *121*, 465–474.
(61) Sing, K. S. W.; Everett, D. H.; Haul, R. A. W.; Moscou, L.; Pierotti, R. A.; Rouquerol, J.; Siemieniewska, T. *Pure Appl. Chem.* **1985**, *57*, 603–619.
(62) Rouquerol, F.; Rouquerol, J.; Sing, K. *Adsorption by Powders and Porous Solids: Principles, Methodology, and Applications*; Academic Press: San Diego, 1999.

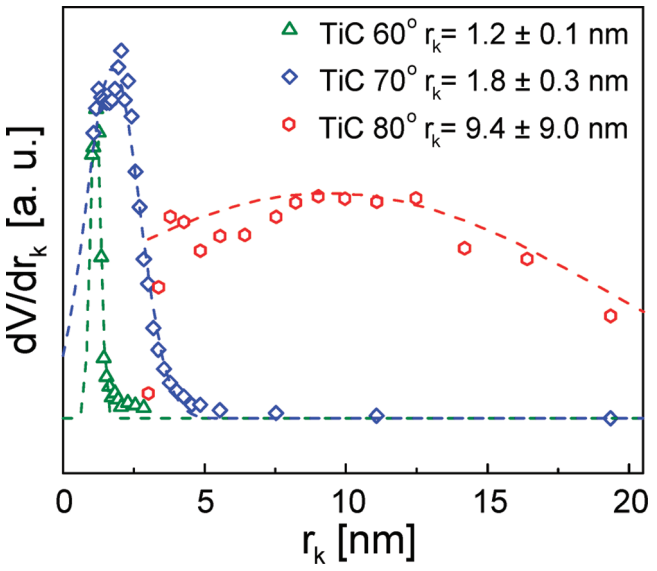

Figure 7. Mesopore size distribution as determined from the desorption branch of toluene adsorption isotherms on TiC films deposited at 60° (Δ), 70° (◇), and 80° (○).

greater for TiC 13° compared to the bare QCM or TiO_2 13°, both of which are nonporous. The greater adsorption capacity of the TiC 13° film arises due to toluene adsorption within micropores. This means that the BET *C* value of 108, which taken by itself would indicate high adsorption energy for toluene, is artificially inflated by the presence of the micropores.[62] This is consistent with our previous work on TiO_2, recall that the TiC surface is largely oxidized, which also indicated low C values for toluene adsorption on mesoporous TiO_2.[39,63] The isotherm also exhibits a significant hysteresis at low partial pressures which is attributed to trapping of adsorbate molecules in micropores.[62] A subsequent adsorption−desorption cycle on TiC 13°, shown in Figure 6b, demonstrated a lack of adsorption at low partial pressures and exhibited a shape similar to a Type II isotherm with much lower mass adsorption.[62] Additionally, the calculated *C* value approached a value of one which is consistent with adsorption on a nonporous substrate with very weak adsorbate−adsorbent attraction. The irreversible isotherms evident on TiC 13° contrast sharply with measurements made on samples grown at higher deposition angles. Subsequent adsorption−desorption cycles on samples deposited at angles from 50 to 85° are nearly identical with the initial cycle, excepting a small amount of irreversible adsorption in the micropore region, $P/P_o < 0.05$. For clarity of presentation, only the first and second adsorption−desorption cycles for the TiC film deposited at 70° are presented in Figure 6e which are representative of the repeatability of the other isotherms. In summary, adsorption data for TiC deposited at 13° is consistent with irreversible toluene adsorption inside very narrow micropores during the first adsorption cycle, after which the second cycle indicates very weak interaction between toluene and the external surface.

(63) Patel, M. N.; Williams, R. D.; May, R. A.; Uchida, H.; Stevenson, K. J.; Johnston, K. P. *Chem. Mater.* **2008**, *20*, 6029–6040.

Isotherms of toluene adsorption on TiC deposited at 50° (Figure 6c) are also consistent with Type I isotherms. These isotherms indicate a diminished low pressure hysteresis in comparison to the 13° film, as well as an increase in the total volume fraction of toluene adsorbed. These changes suggest that the 50° deposition angle templates slightly larger micropores which do not trap toluene as readily as those within the 13° films. Deposition at 60° results in isotherms that exhibit significant adsorption at low pressure; however, these films now include a hysteresis loop extending from $P/P_o \approx 0.1-0.4$, Figure 6d. Repeatable hysteresis loops at these higher partial pressures are associated with capillary condensation in mesopores, which are defined as pores between 2 and 50 nm in diameter.[62] The volume fraction adsorbed continues to increase as the deposition angle increases to 70° and 80°, as shown in Figure 6e,f. Additionally, the hysteresis loop of these films broadens and shifts to higher partial pressures, consistent with an increase in the mean pore diameter with increasing deposition angle. The shape of the hysteresis loops become increasingly elongated resembling that of a Type H3 hysteresis which suggests adsorption between plate like particles.[62] This observation is consistent with the SEM images shown in Figure 1 indicating that at deposition angles of 60° and greater the film is comprised of closely spaced nanocolumns with roughly elliptical cross sections. As observed in SEM, increases in the deposition angle from 60° to 85° lead to greater separation between the nanocolumns which are reflected in the corresponding toluene isotherms.

The Kelvin equation: $r_K = \frac{-2\gamma V_m \cos(\theta)}{RT \ln(P/P_0)}$ was employed to qualitatively evaluate the mesopore size distribution (PSD). In the case of toluene adsorption, $\gamma = 0.0284$ $N \cdot m^{-1}$, $V_m = 1.06 \times 10^{-4}$ $m^3 \cdot mol^{-1}$, $\theta = 0$, $R = 8.314$ $J \cdot mol^{-1} \cdot K^{-1}$, and $T = 290$ K. Figure 7 presents the PSD derived from the desorption branch of the isotherms performed on the 60°, 70°, and 80° samples. The limitations of the Kelvin equation are widely known, especially with mesopores in the 2−10 nm size range. Therefore, for the 60° film, we cannot rule out that the sudden decrease in the desorption branch is due to the tensile strength effect. Despite this possibility, the desorption branch was used to determine all pore size distributions. The adsorption branch provides similar results, but the resulting PSD is much broader making it difficult to visualize the changes in the average pore size due to the deposition angle. In previous work, we have found very good agreement between the pore diameter determined by the Kelvin equation and SEM and XRD measurements for porous TiO_2 films.[39] However, because of the potential for ambiguity, results are discussed only in terms of the Kelvin radius and not the pore size (or pore diameter). These measurements show the dramatic dependence of the TiC film morphology on the deposition angle. The Kelvin radius, r_K, increases from 1.2 ± 0.1 nm for the 60° deposition to 1.8 ± 0.3 nm for the 70° deposition and 9.4 ± 9.0 nm for the 80° deposition. Fine control of the pore structure of these films is important for a variety of the applications of TiC or other metal carbides. At these

Table 1. BET and α_s Analysis of Deposition Angle-Templated TiC Samples

dep. angle (°)	BET S.A. ($m^2 \cdot g^{-1}$)	C	micropore volume fraction	mesopore volume fraction	α_s S.A. ($m^2 \cdot g^{-1}$)
13	14	108	0.05	0	10
50	30 ± 10	180 ± 70	0.07	0	10
60	100 ± 30	32 ± 8	0.08	0.07	410
70	180 ± 50	21 ± 4	0.09	0.27	710
80	240 ± 30	23 ± 6	0.04	0.52	240

size ranges, quantum effects may dominate with small changes in the size of columns potentially having great effect on material properties.[64] Additionally, for applications in catalysis where high surface area TMCs are frequently employed, postsynthesis deposition and distribution of nanoparticles inside the porous network will be strongly dependent on pore size.[39] Further, direct control of the pore sizes of carbides for the production of porous carbide-derived carbons used for electrochemical capacitors will certainly affect the porous architecture of the resulting carbons having a profound effect on their performance.[65]

While the Brunauer−Emmett−Teller (BET) method is perhaps the most popular technique for determining the specific surface area (SSA) of high surface area media, the BET method is generally considered inaccurate for samples with weak interaction between the adsorbate and surface or materials which contain significant microporosity. Specifically, if the formation of a complete adsorbate monolayer cannot be distinguished from the onset of multilayer adsorption (indicated by low C values) or if the monolayer formation coincides with micropore adsorption, then the BET monolayer capacity cannot be determined accurately. Lack of a well-defined monolayer capacity introduces significant uncertainty into SSA values. These limitations do not allow for the application of the BET method to determine the monolayer adsorption capacity from adsorption isotherms reported in this study. On the other hand, application of the BET method is still instructive for comparison with more traditional studies and for determining the BET C values, which can indicate the presence of microporosity. For this purpose, SSA and C values for the films have been estimated using the BET method (applied over the range P/P_o = 0.05−0.35) and are displayed in Table 1. The calculated BET surface areas increase with increasing deposition angle from 14 $m^2 \cdot g^{-1}$ to 240 $m^2 \cdot g^{-1}$; an increase that displays a high degree of linearity ($R^2 > 0.99$) from 50° to 80°. This contrasts with our previous investigation of TiC films deposited using RBD. In the prior study, cyclohexane was adsorbed on the films at 140 K under ultrahigh vacuum to quantify the adsorption capacity which was employed to calculate the specific surface area using a known standard. The surface area reached a maximum of 840 $m^2 \cdot g^{-1}$ at a deposition angle of 65° and deposition temperature of 77 °C.[25] In the previous study, deposition at an angle of 65° and temperature of 27 °C (more comparable to this study) resulted in a specific surface area of ~700 $m^2 \cdot g^{-1}$.[25] Clearly, this value is much larger than the maximum value of 240 $m^2 \cdot g^{-1}$ determined by BET analysis of toluene adsorption presented here. Further, the BET method indicates that the film deposited at an angle of 80° has the highest surface area, whereas previous work demonstrated that the maximum value should occur between 60° and 70°.

Differences in the surface area measurements between the two studies are easily resolved by employing an alternative analysis of the isotherms, presented here. The α_s method, developed by Sing and co-workers, is an empirical technique that can be confidently applied to a broad array of isotherms so long as a reference isotherm on a chemically similar nonporous material has been obtained.[62] To monitor adsorption mechanisms on the porous TiC samples, a reference isotherm was generated by depositing a TiO_2 13° film using a similar RBD method (TiC 13° films were unsuitable due to the large hysteresis at low pressures).[24] Additional discussion of the α_s technique and its implementation as well as the reference isotherm and the calculated α_s plots are contained in the Supporting Information and Figure S7. Values for the surface area as well as micropore and mesopore volumes calculated by the α_s method are displayed in Table 1. As seen in Table 1, the volume ratio of mesopores to micropores increases with deposition angle from ~1:1 for the 60° film to ~13:1 for the 80° film. Due to a low C value (characteristic of Type III isotherms and indicating an unreliable value for the monolayer capacity), the surface area of the TiO_2 reference sample could not be determined by BET methods. Therefore, the relative surface areas were converted to absolute surface areas using the BET value obtained for the 80° sample. The 80° isotherms were close to ideal Type IV isotherms with low micropore volumes and exhibited very linear ($R^2 > 0.999$) BET plots from P/P_o = 0.05 to P/P_o = 0.50, suggesting that it closely adheres to the BET model. The α_s surface area values are considered external surface areas because they do not include contributions from micropores. Values of the external SSA for TiC films calculated by the α_s method are displayed in Table 1. The maximum SSA for the deposited TiC films was 710 $m^2 \cdot g^{-1}$ for TiC 70°. This value closely corresponds to the value of ~700 $m^2 \cdot g^{-1}$ observed for TiC films deposited at an angle of 65° and 27 °C in the previous study.[25] Additionally, SSA values for TiC 60° and TiC 80° are in general agreement with values from the previous study. In comparison, the TiC 13° and TiC 50° films have much smaller surface areas than the mesoporous samples. This is expected since the porosity, and thus most of the surface area, observed for these films is due to the presence of micropores which are expressly excluded from α_s analysis which only takes into account external surface area.

(C). Comparison of Isotherms Derived from QCMP and EP. Ellipsometric porosimetry (EP) utilizes ellipsometry to monitor changes in the refractive index and thickness of a sample as it is exposed to increasing concentrations of an adsorbate. However, neither quartz crystal

(64) May, R. A.; Kondrachova, L.; Hahn, B. P.; Stevenson, K. J. *J. Phys. Chem. C* **2007**, *111*, 18251–18257.
(65) Simon, P.; Gogotsi, Y. *Nat. Mater.* **2008**, *7*, 845–854.

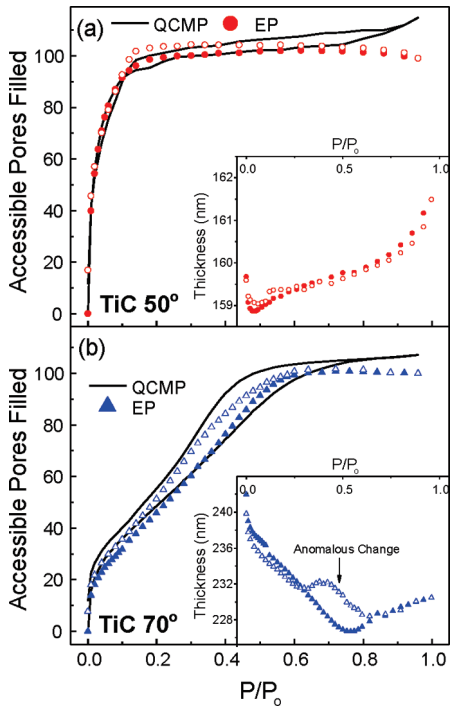

Figure 8. Comparison of the fraction of accessible pores filled by the toluene adsorbate versus partial pressure determined by EP (symbols) and QCMP (lines) for TiC deposited at angles of (a) 50° and (b) 70°. Insets depict the thickness change determined by EP; note in (b) the desorption branch depicts an anomalous thickness increase observed for all isotherms with hysteresis loops.

microbalance porosimetry (QCMP) nor ellipsometric porosimetry (EP) directly measure the mass of adsorbate on a porous sample. For QCMP, the measured quantity is the dampening of the resonant frequency of the quartz oscillator during adsorption. Generally, the conversion of Δf_R to mass is relatively straightforward via the Sauerbrey equation.[40] The EP data were much more difficult to interpret due to large absorption of light by the TiC samples across the measured spectral range and a high degree of optical anisotropy for films deposited at angles greater than 50°. Toluene does not absorb light in the 300−1000 nm range, so initial attempts were made to keep the k values determined at $P/P_o = 0$ constant (by holding the amplitude and broadening of the optical model's Lorentzian oscillators constant) and only fit for changes in n and thickness by adding a Cauchy dispersion equation to the series of Lorentzian oscillators describing the TiC.[54] This approach did not result in acceptable fits to the ellipsometry data for any of the deposition angles and was abandoned. Therefore, n, k, and thickness (a total of eight total fit parameters) were allowed to change during fitting of the SE data from 300 to 1000 nm. This method resulted in good fits to the SE data but caused concerns over parameter correlation and raised the question of why k would change at all. We speculate that the measured change in k is an anomaly of the fitting procedure and not an expression of vapochromic properties of the TiC samples. However, further studies are underway utilizing similarly deposited TiO_2, which is transparent in the visible wavelength region, to understand this phenomenon along with the application of generalized ellipsometry which can more adequately describe anisotropic samples.[66,67]

Despite these difficulties, a method utilizing BEMA was successfully employed to compare the EP and QCMP data, as shown in Figure 8. In this implementation, it was assumed that the EP data at a given partial pressure could be described by a mixture of the complex refractive index at $P/P_o = 0$ and the complex refractive index determined just after pore saturation ($P/P_o = 0.30$ for TiC 50° and $P/P_o = 0.64$ for TiC 70°). The thickness of the film and the fractional contribution of the saturated film were the only two fit parameters. The resulting fraction gives the amount of accessible porosity that has been filled by adsorbate, as shown by Sanchez et al.,[68] and can be compared to the QCMP data acquired at the same time. For the TiC 50° sample, Figure 8a, agreement between the two methods is excellent, differing by an average of only 1% before saturation at $P/P_o = 0.30$. At higher partial pressures, the values diverge, especially above $P/P_o = 0.80$. This divergence was observed in every film for which a saturated plateau was observed; i.e., TiC 13°, TiC 50°, TiC 60°, and TiC 70°. This region corresponds to multilayer formation on the surface of the TiC. The QCM detects these multilayers as a mass change and the isotherm curves upward at higher partial pressures consistent with multilayer formation. In contrast, the EP isotherm remains constant or decreases slightly after saturation. Recall that this isotherm is determined only by accounting for changes in the complex refractive index and not the measured thickness values. Once the open porosity ($n_{nitrogen} = 1$) of the film has been replaced by toluene ($n_{toluene} = 1.44$) there are no additional changes in the refractive index of the sample with further increases in P/P_o. The small changes in refractive index as the toluene forms multilayers on the surface are negligible compared to the refractive index of the film. However, this does not mean that the additional adsorption is undetectable. Note the inset to Figure 8a; the measured thickness increases at higher partial pressures and has a shape that is similar to that seen in the QCMP data. Thus, ellipsometry is capable of detecting the multilayer adsorption, via shifts in Δ, but it is seen as a thickness change and not a change in the complex refractive index. This subtle difference in detection is important when analyzing EP data, especially concerning α_s plots which rely on the shape of the isotherm to determine parameters such as pore volume and surface area.

Analysis of the ellipsometrically derived thickness changes reveals other interesting phenomenon as well. The thickness of the 50° sample decreases slightly at low toluene partial pressures due to capillary condensation within this film. This observation is in contrast to the apparent thickness of the TiC 13° and TiO_2 13° films

(66) Gospodyn, J.; Sit, J. C. *Opt. Mater.* (*Amsterdam, Neth.*) **2006**, *29*, 318–325.
(67) Schmidt, D.; Booso, B.; Hofmann, T.; Schubert, E.; Sarangan, A.; Schubert, M. *Appl. Phys. Lett.* **2009**, *94*, 011914/1–011914/3.
(68) Boissiere, C.; Grosso, D.; Lepoutre, S.; Nicole, L.; Bruneau, A. B.; Sanchez, C. *Langmuir* **2005**, *21*, 12362–12371.

(Supporting Information, Figure S8), which increase monotonically throughout the entire pressure range due to multilayer formation on the film surface. Recall that the increased reversibility of toluene adsorption on TiC 50°, in comparison to TiC 13°, was attributed to enlarged micropores templated by the 50° deposition angle which do not trap toluene as readily as the smaller micropores within the 13° film. Condensation inside these larger micropores can form a meniscus, the associated capillary forces which cause the decrease in film thickness seen in the inset of Figure 8a. Capillary adsorption in large micropores has been observed and is further evidence that deposition at 50° results in larger micropores than deposition at 13°.[62]

EP and QCMP isotherms taken on TiC 70° are indicative of isotherms obtained at other angles. As the partial pressure of toluene is increased, agreement between the adsorption branches as measured by EP and QCMP for TiC 70° (Figure 8b) is good, although it diverges in the multilayer adsorption region due to the factors discussed above. As expected, the overall thickness of the entire film decreases as mesopores are filled and the resulting capillary forces increase leading to a ~10% decrease in film thickness. Following the completion of capillary condensation, the film thickness increases due to a combination of relaxation of the capillary forces and multilayer formation at high partial pressures, $P/P_o > 0.75$. As the partial pressure of toluene is decreased during the desorption branch, the EP data diverge by as much as 8% from the QCMP data. This divergence is accompanied by an unexpected increase in the thickness measured by EP (Figure 8b inset). At $P/P_o < 0.60$, the hysteresis loop closes and the agreement between EP and QCMP improves considerably. Similar anomalies in the ellipsometricly derived thickness were observed in the hysteresis loop region of all Type IV isotherms taken in this study and under certain fitting conditions in a previous study of TiO_2.[39] Thin film stress effects are known to impact the response of QCMs;[69] therefore, one possibility for this difference is that stress associated with capillary forces due to the toluene condensation within the films' pores affected the f_R of the QCM, producing anomalous QCMP results. To determine if stress was a factor, similar TiC films were deposited at 50°, 60°, and 70° on BT cut quartz crystals. BT cut crystals have a stress response that is approximately equal in magnitude to AT cut crystals but opposite in sign. Therefore, differences between isotherms of identical films deposited on each crystal type can be used to determine the contribution of stress to the frequency response.[69] Isotherms conducted on TiC 50°, TiC 60°, and TiC 70° deposited on AT and BT cut quartz were within experimental error of film deposition (Supporting Information, Figure S9), so adsorbate induced stress in the QCM crystal is not a significant contributing factor, although subtle effects would not be detected due to variations in the deposited films. Thus, the difference in the QCMP and EP isotherms is most likely due to errors associated with the analysis of the ellipsometry data. The difference can be ascribed to high parameter correlation between the thickness and BEMA fraction parameters though the resulting fits were independent of seed values, and it is odd that correlation issues would only arise in a specific portion of the isotherm. One possibility is that the ellipsometry parameters are more sensitive to stress than the QCM crystals, although further study is necessary to conclusively determine the origins of these EP anomalies.

(69) EerNisse, E. P. *J. Appl. Phys.* **1973**, *44*, 4482–4485.

(D). Summary. We have studied the synthesis of high surface area, porous, and thermally robust titanium carbide films created by the reactive ballistic deposition technique. Notably, this deposition technique leads to the formation of titanium carbide at unprecedented temperatures, 35 °C, as illustrated using X-ray diffraction and X-ray photoelectron spectroscopy measurements. Quartz crystal microbalance porosimetry (QCMP) and ellipsometric porosimetry (EP) were used to characterize the morphology of these films, and general agreement between the two methods was observed. Comparison of the two methods also revealed important subtleties in the analysis of the porosimetry data. The hybrid porosimetry approach extends the use of SE-based porosimetry toward optically absorbing materials. In this case, porosimetry measurements quantitatively show that control and variation of a single parameter, deposition angle, allows for direct tailoring of the films' optical constants, porosity, surface area, and pore size distribution. The specific surface area of the TiC samples varied from 10 to 710 $m^2 \cdot g^{-1}$ for films deposited between 13 and 80°. Films grown with a deposition angle of 60° had an average Kelvin radius of 1.2 nm while a deposition angle of 70° resulted in films with an average Kelvin radius of 1.8 nm. RBD deposition of TiC has resulted in great control over important properties such as surface area, refractive index, porosity, and pore size distribution resulting in materials with applications as catalysts or optical coatings. These unique materials were successfully characterized using a novel combined QCM and ellipsometric porosimetry technique which simultaneously determines the refractive index and mass addition under various partial pressures.

Acknowledgment. C.B.M. acknowledges the Defense Threat Reduction Agency (CBT070005974), the Army Research Office (W911NF-09-1-0130), the National Science Foundation (CTS-0553243), and the Welch Foundation (F-1436) for their generous support. K.J.S. acknowledges the Welch Foundation (F-1529) and the National Science Foundation (CHE-0809770). D.W.F. would like to acknowledge the Bruce B. Jackson Endowed Graduate Fellowship in Engineering. The Kratos XPS was funded by the National Science Foundation under Grant CHE-0821312.

Supporting Information Available: Additional experimental details; tabulated TiC crystallites sizes; fit parameters for the ellipsometric models; additional XRD and XPS data; discussion and illustration of the α_s analysis; and a comparison of the adsorption induced responses for TiC films deposited on AT and BT cut QCM crystals (PDF). This material is available free of charge via the Internet at http://pubs.acs.org.